COMMUNICATION

Check for updates

Structure and magnetism of mixed-valent iron oxysulfides $Sr_3Fe_4O_6S_2$ ($Sr_3(Fe^{3+})_2O_5(Fe^{2+})_2OS_2$) and $Sr_4Fe_4O_7S_2$ ($Sr_4(Fe^{3+})_2O_6(Fe^{2+})_2OS_2$)

Alexis N. Gillette,[a] Annabel R. Lyon, [ID][a] Stanislav Savvin,[bc] Ines Puente-Orench,[b] Sepideh Rahimisheikh,[d] Joke Hadermann, [ID][d] Magali Gimeno,[a] Michael L. Neidig [ID][a] and Simon J. Clarke [ID] *[a]
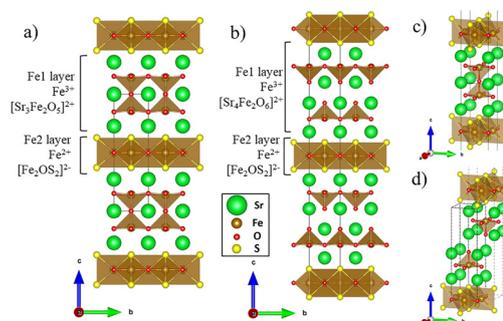
The crystal and magnetic structures of $Sr_3Fe_4O_6S_2$ ($\equiv Sr_3Fe_2O_5Fe_2OS_2$) and $Sr_4Fe_4O_7S_2$ ($\equiv Sr_4Fe_2O_6Fe_2OS_2$), designed using a building-block approach, are reported. They are fully charge-ordered with Fe^{2+} and Fe^{3+} ions in distinct layers showing independent long-range magnetic order. Complex microstructures in some regions suggest new targets.

Mixed-anion compounds are a growth area of solid-state chemistry. Layered structures are often adopted due to anion ordering and desirable properties include tuneable bandgap energies for semiconductors,[1] promising thermoelectric properties,[2] high-temperature superconductivity[3] and complex magnetism.[4] A fruitful design method for oxide chalcogenides[5] is to use as building blocks individual layers or slabs found in known compounds, and combine them in new ways to target new structures and compositions. We proposed new targets containing the strontium iron oxide slabs from $Sr_3Fe_2O_5Cu_2S_2$ or Sr_2FeO_3CuS[6] combined with the iron oxide sulfide layer in $Sr_2F_2Fe_2OS_2$.[7] The similar basal lattice parameters of these compounds suggested 1:1 intergrowths might form.

These targets, conveniently formulated as $Sr_3Fe_2O_5Fe_2OS_2$ (compound **1**) and $Sr_4Fe_2O_6Fe_2OS_2$ (**2**), were synthesized in high purity from SrO, Fe_2O_3, Fe, and S by ceramic solid-state synthesis in alumina crucibles within evacuated sealed fused silica tubes heated at 1 °C per minute to 900 °C (enabling sulfur to react before attaining a high vapour pressure) with a dwell time of 48 hours resulting in black powders stable to ambient air. Full synthetic details are in the SI. Structural models were devised by constructing 1:1 intergrowths as indicated above, with appropriate interatomic distances, and these accounted well for the powder diffraction patterns of both new products.

Both phases contain iron in distinct Fe1 and Fe2 layers and in two different coordination environments: a square pyramidal $[FeO_5]$ unit (Fe1—initially assumed to contain Fe^{3+}) and a distorted octahedral $[FeO_2S_4]$ unit with O atoms arranged *trans* to one another (Fe2—initially assumed to contain Fe^{2+}). **1** crystallizes in the primitive tetragonal space group $P4/mmm$ with layers of basal-vertex-linked $[FeO_5]$ pyramids joined *via* apical oxide vertices to form double-thickness layers of $[FeO_5]$ pyramids (Fig. 1a). **2** (Fig. 1b) crystallizes in the body-centred tetragonal space group $I4/mmm$ with adjacent layers of basal-vertex-linked $[FeO_5]$ pyramids separated and shifted by $(a + b)/2$ in the basal plane, effectively by the insertion of a rock salt layer SrO into the oxide slab present in **1** (Fig. 1c and d). In addition to the different Fe-sites within the phases, there are also different sites occupied by the Sr^{2+} cations, 12- and 8-coordinate sites in **1** and 9- and 8-coordinate sites in **2** (Fig. S2).

Fig. 2 shows Rietveld refinements against synchrotron X-ray powder diffraction (XRPD) patterns (beamline I11 (Diamond Light Source (DLS))) (Table 1).[8] Neutron Powder Diffraction (NPD) used beamlines D1B, D2B, and XtremeD at the Institut Laue Langevin (ILL)[9–11] to better locate O atoms (Fig. S1 and

[a] *Department of Chemistry, University of Oxford, Inorganic Chemistry Laboratory, South Parks Rd, Oxford, OX1 3QR, UK. E-mail: simon.clarke@chem.ox.ac.uk*

[b] *Institut Laue-Langevin, 71 Avenue des Martyrs, 38000, Grenoble, France*

[c] *Instituto de Nanociencia y Materiales de Aragón, CSIC – Universidad de Zaragoza, Facultad de Ciencias C/Pedro Cerbuna 12, Zaragoza, Spain*

[d] *Electron Microscopy for Materials Science (EMAT), University of Antwerp, Groenenborgerlaan 171, B-2020, Antwerp, Belgium*

Fig. 1 Crystal structures of (a) **1**: $Sr_3Fe_2O_5Fe_2OS_2$ ($\equiv Sr_3Fe_4O_6S_2$) and (b) **2**: $Sr_4Fe_2O_6Fe_2OS_2$ ($\equiv Sr_4Fe_4O_7S_2$). (c) shows apically connected FeO_5 pyramids in **1** and (d) shows separation of these pyramids by insertion of SrO in **2**.
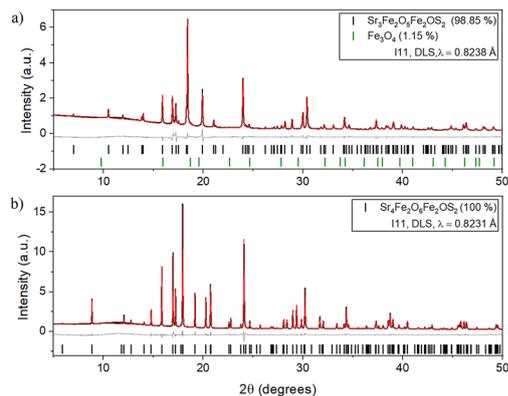
Fig. 2 Rietveld refinements (300 K) against XRPD patterns (I11, DLS) of (a) **1**: $Sr_3Fe_2O_5Fe_2OS_2$ (R_{wp} = 3.956%) and (b) **2**: $Sr_4Fe_2O_6Fe_2OS_2$ (R_{wp} = 4.811%). Observed (black), calculated (red) and difference (grey) curves are shown. See also Table 1 and Table S1.

Tables S1b and S2). Refinements showed that all sites were fully occupied within the uncertainties of the refinements. Fe–O and Fe–S bond lengths indicated the more oxophilic Fe^{3+} in the [FeO_5] square pyramids and Fe^{2+} ions in the [FeO_2S_4] octahedra.

NPD data from D1B (Fig. 3) were used to deduce the magnetic structure of **1**. Low-angle peaks of magnetic origin, present at 300 K, gain little intensity on cooling, indicating magnetic long-range order (LRO) well above room temperature. Further magnetic reflections below 115 K indicate further magnetic ordering (Fig. 3b). At 300 K, the magnetic peaks of **1** can be indexed on a $\sqrt{2}a \times \sqrt{2}a \times 2c$ expansion of the nuclear cell and testing of possible antiferromagnetic models revealed that the intensities could be fully accounted for by LRO of only the Fe^{3+} ions on the Fe1 sites. Within each [$Sr_3Fe_2O_5$]$^{2+}$ slab, Fe^{3+} moments order antiferromagnetically *via* Fe–O–Fe 163.7° super-exchange interactions involving the bases of the square pyramids and are oriented within the basal plane. The Fe1 moments are also coupled antiferromagnetically *via* 180° Fe–O–Fe super-exchange through shared apical oxides. This ordering is similar to that in the related $Ae_3Fe_2O_5Cu_2Ch_2$ (Ae = Ba, Sr, Ca; Ch = S, Se).[12,13] The long-range ordered moment saturates at 4.07(5)μ_B per Fe1 in **1** below 160 K, diminished from the expected 5μ_B for a high-spin d^5 Fe^{3+} cation due to covalency.

NPD may, in principle, not always provide a unique magnetic model.[14] In **1** a single-phase magnetic model at 300 K has Fe1 moments collinear within a slab, but rotated in adjacent slabs by 73° relative to one other (Fig. 4b); this rotation angle increases to 85° at 5 K. A two-phase model indistinguishable by powder diffraction is discussed in the SI. The Fe^{2+} ions on the

Table 1 300 K unit cell information for $Sr_3Fe_2O_5Fe_2OS_2$ (**1**) and $Sr_4Fe_2O_6Fe_2OS_2$ (**2**)

	1 – $Sr_3Fe_2O_5Fe_2OS_2$	**2** – $Sr_4Fe_2O_6Fe_2OS_2$
Space group	$P4/mmm$ (No. 123)	$I4/mmm$ (No. 139)
a (Å)	3.9615(6)	3.945892(8)
c (Å)	13.519(9)	31.9730(1)
V (Å³)	212.18(1)	497.822(3)
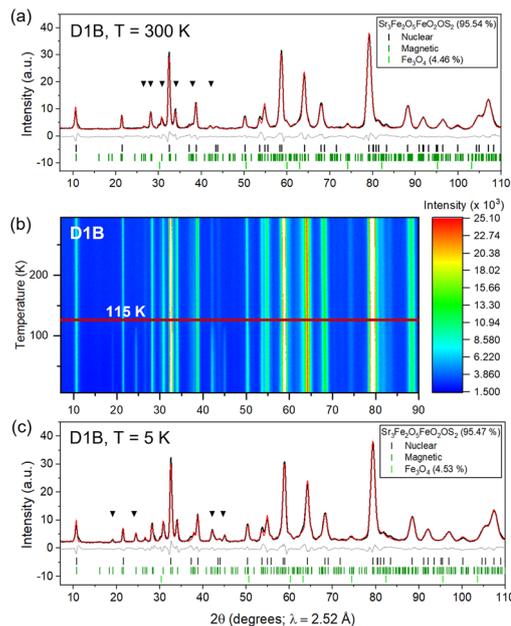
Fig. 3 NPD patterns D1B (ILL) and Rietveld fits for $Sr_3Fe_2O_5Fe_2OS_2$ (**1**) at (a) 300 K (R_{wp} = 6.993%) here black triangles indicate magnetic reflections, (b) 5 K < *T* < 300 K, and (c) 5 K (R_{wp} = 7.602%) here black triangles indicate magnetic reflections emerging below 115 K. Observed (black), calculated (red) and difference (grey) curves are shown.

Fe2 sites in **1** show magnetic LRO below 115 K. New magnetic peaks saturated at 5 K were indexed on a $2\sqrt{2}a \times 2\sqrt{2}a \times 2c$ expansion of the nuclear cell. The ordering scheme (Fig. 4c) was deduced by comparison with related compounds and the magnitude of the long-range ordered Fe^{2+} moments (3.33(7)μ_B) are similar in phases containing exclusively these magnetic layers: $La_2O_2Fe_2OS_2$ (3.30(4)μ_B),[15] $Sr_2F_2Fe_2OS_2$ (3.3(1)μ_B),[16] and $La_2O_2Fe_2OSe_2$ (3.50(5)μ_B).[17]

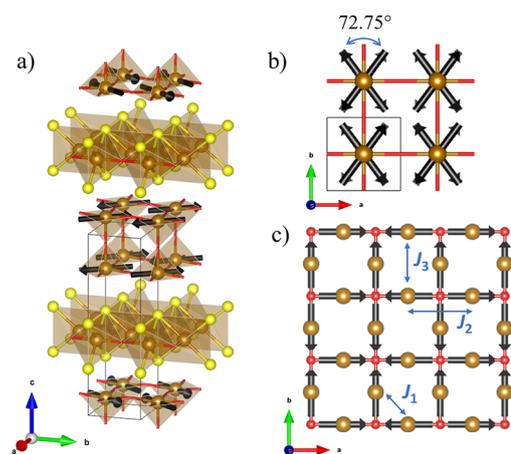**Fig. 4** (a) Refined magnetic structures for $Sr_3Fe_2O_5Fe_2OS_2$ (**1**) at 300 K (Fe1 order with a $\sqrt{2}a \times \sqrt{2}a \times 2c$ supercell expansion; nuclear cell is outlined). (b) Rotation between spins in adjacent Fe1 double layers required for a single-phase model (see SI for an equivalent 2-phase model). (c) Fe2 layer ordering found in both **1** and **2** within the *ab* plane with exchange pathways indicated.
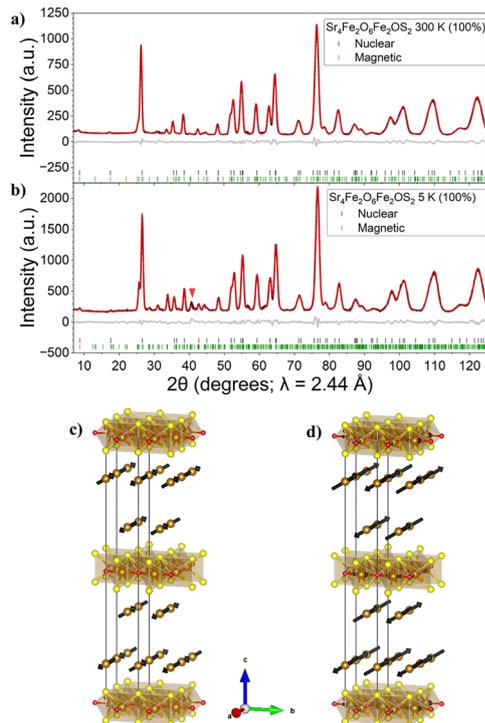
ChemComm

Fig. 5 Rietveld refinements for $Sr_4Fe_2O_6Fe_2OS_2$ (**2**) (NPD data (XtremeD, ILL) at (a) 300 K (R_{wp} = 4.75%) and (b) 5 K (R_{wp} = 4.08%); observed (black), calculated (red) and difference (grey) curves are shown, and the red triangle indicates an asymmetric magnetic peak (see text). (c) 300 K and (d) 5 K magnetic structures; nuclear cell is outlined.

The magnetic structure of **2** was determined by NPD (300 K on *GEM* (ISIS facility) (Fig. S12) and on cooling on XtremeD (Fig. S13) and D2B at ILL (Fig. S1c, S1d and Table S3)). Like in **1**, only Fe^{3+} cations (Fe1) are ordered at room temperature with magnetic peaks indexed on a $\sqrt{2}a \times \sqrt{2}a \times c$ supercell. Antiferromagnetic ordering of Fe1 moments within the sheets of basal-vertex-sharing [FeO$_5$] square pyramids was found to be similar to that in **1**, but separation of the sheets by insertion of an SrO layer into the oxide slabs and the loss of the strong Fe–O$_{axial}$-Fe superexchange means the ordered moment (2.14(2)μ_B) is unsaturated at 300 K, but it saturates at 3.7(2) per Fe^{3+} ion (comparable to in **1**) at 5 K. The Fe1 moments in **2** are best modelled as tilted from the *c* axis by 56(1)° at 5 K. As in **1**, other related models are indistinguishable in a powder measurement (see SI). Note that high-spin d^5 moments, as on the Fe1 sites in **1** and **2**, have very weak directional preference.[18] The Fe2 site moments on Fe^{2+} cations in the Fe$_2$O sheets of **2** order below 150 K in a similar pattern to that in **1** on a $2\sqrt{2}a \times 2\sqrt{2}a \times c$ expansion of the nuclear cell (see Fig. S14). The Fe^{2+} moment refines to 2.1(1)μ_B at 5 K, somewhat lower than in **1**. In **2**, there is a mismatch in the Rietveld refinement at 5 K for an asymmetric magnetic peak around 40.6° in the XtremeD data (red triangle in Fig. 5b) arising from the Fe2 magnetic ordering. This also appears in related body-centred compounds containing [Fe$_2$OS$_2$] layers (*e.g.* La$_2$O$_2$Fe$_2$OS$_2$)[15] and has been attributed to intrinsic stacking faults in the magnetic structure as explained in ref. 15.
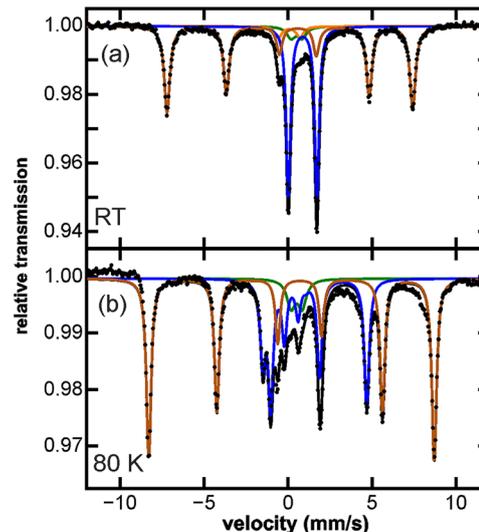

Fig. 6 ^{57}Fe Mössbauer spectra for tetragonal $Sr_3Fe_2O_5Fe_2OS_2$ (**1**) at room temperature (RT) (a) and 80 K (b). Fe1 (Fe^{3+}) (Brown) is magnetically ordered a both temperatures, producing sextets from the magnetic hyperfine interaction and Fe2 (Fe^{2+}) (Blue) undergoes long-range magnetic ordering below 115 K (according to NPD), and in this case the sextet is highly asymmetric as found in compounds with related motifs.[7,19] The origin of the lower population doublet (Green) required to fit the data at both temperatures, and the second minority orange doublet at RT is uncertain. Fitting parameters are in Table S4.

^{57}Fe Mössbauer spectroscopy measurements (see SI for details) on $Sr_3Fe_2O_5Fe_2OS_2$ (**1**) are consistent with the PND results, showing independent magnetic ordering on the Fe1 and Fe2 sites. At room temperature there is a sextet due to the ordered Fe1 moments (isomer shift (δ) of 0.34 mm s^{-1} suggesting Fe^{3+}) and a doublet from the Fe2 moments (δ = 0.87 mm s^{-1} suggesting Fe^{2+})[19] plus two minority doublet components of uncertain origin (but see below). At 80 K (Fig. 6b), the ordered Fe2 moments give a highly asymmetric sextet quantitatively similar to those in $Ba_2F_2Fe_2OSe_2$, $Sr_2F_2Fe_2OS_2$[7] and Nd_2O_2-Fe$_2$OSe$_2$[19] with related [Fe$_2$OS$_2$] layers, and one of the minor doublets (δ = 0.51 mm s^{-1} suggesting Fe^{3+}) remains (6%).

Some samples of **1** were found to show broad additional features in the powder diffraction patterns (Fig. S3(a)) and others were found, using synchrotron X-ray powder data, to undergo subtle distortions which can be modelled by reducing the symmetry to orthorhombic below 500 K (Fig. S3(b) and S4), and this was sometimes induced by lengthy annealing. Preliminary transmission electron microscopy (TEM) measurements (Fig. 7) on a sample of **1** which was tetragonal at all temperatures and did not show any broad features in the powder diffraction patterns nevertheless show the presence of diverse stacking faults which may account for the minority Mössbauer components, and the occurrence of ubiquitous Fe$_3$O$_4$ impurities. These faults include translational faults along the stacking direction (Fig. 7b and d) and thicker Fe1-layer-related blocks (Fig. 7e), and may suggest new targets and options for compositional and structural tuning. Variation in such features between samples may be responsible for the broad peaks in the diffractograms of some
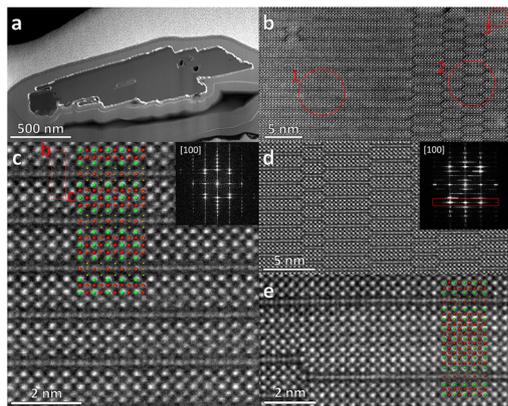
Fig. 7 High-Angle Annular Dark Field (HAADF) Scanning Transmission Electron Microscopy (STEM) images of a tetragonal crystal of **1** prepared using Focussed Ion Beam (FIB) milling in a slice perpendicular to the *a*-axis (a), to enable imaging along the [100] direction. (b) shows the occurrence in the same crystallite of well-crystallised regions consistent with the average structure (region 1 see (c)), and regions of complex defects. Region 2 and (d) shows blocks translated by *c*/2, in regular ways, while region 3 and (e) shows a much thicker Fe1-type slab.

samples and the reduction in symmetry in others (see Fig. S5 for images of a sample of **1** that is orthorhombic, or lower, by PXRD at RT) and requires further detailed investigation. Such stacking faults have been noted in related compounds such as $Sr_2FeO_{3-}CuSe$.[20] From preliminary TEM measurements (Fig. S7), compound **2** seems less prone to such defects or impurities.

In summary, $Sr_3Fe_2O_5Fe_2OS_2$ (**1**) and $Sr_4Fe_2O_6Fe_2OS_2$ (**2**) have been constructed using building blocks known from existing compounds. Fe^{3+} cations in $[FeO_5]$ square-based pyramids are antiferromagnetically ordered at room temperature and Fe^{2+} cations in *trans*-$[FeO_2S_4]$ octahedra order antiferromagnetically below 115 K and 150 K in **1** and **2** respectively. Single crystal neutron diffraction experiments are required to fully resolve intrinsic ambiguity in the magnetic structures. We have previously identified[21] new targets from analysis of high-resolution HAADF-STEM images, and in the case of **1**, analysis of such images (Fig. 7 and Fig. S5) reveals the occurrence of stacking fault regions as well as perfectly ordered regions showing that these compounds have the capacity to adopt more complex structures. Future work will involve taking inspiration from these images to target new compositions as well as tuning the magnetic interactions and electron counts in **1** and **2** by iso- and aliovalent substitution and topochemical transformations.

ANG: synthesis/analysis for **1**, ARL: synthesis/analysis for **2**. SR and JH: Electron diffraction and TEM imaging/analysis. SS and IPO: NPD data collection at ILL. MG and MLN: Mössbauer data collection/analysis. SJC: materials and initial concepts. ANG drafted the manuscript with input from the other authors.

Conflicts of interest

There are no conflicts to declare.

Data availability

PND data are available at doi:https://doi.org/10.5291/ILL-DATA.5-31-2917 and https://doi.org/10.5291/ILL-DATA.5-31-3008. Other data supporting this article have been included as part of the supplementary information (SI). Supplementary information: additional synthetic and analysis details. https://doi.org/10.1039/d6cc00150e.

Acknowledgements

References

1 K. Ueda and H. Hosono, *J. Appl. Phys.*, 2002, **91**, 4768–4770.
2 S. D. N. Luu and P. Vaqueiro, *J. Mater.*, 2016, **2**, 131–140.
3 Y. Kamihara, T. Watanabe, M. Hirano and H. Hosono, *J. Am. Chem. Soc.*, 2008, **130**, 3296–3297.
4 H. Kageyama, K. Hayashi, K. Maeda, J. P. Attfield, Z. Hiroi, J. M. Rondinelli and K. R. Poeppelmeier, *Nat. Commun.*, 2018, **9**, 772.
5 L. Cario, H. Kabbour and A. Meerschaut, *Chem. Mater.*, 2005, **17**, 234–236.
6 W. J. Zhu and P. H. Hor, *J. Solid State Chem.*, 1997, **134**, 128–131.
7 H. Kabbour, E. Janod, B. Corraze, M. Danot, C. Lee, M.-H. Whangbo and L. Cario, *J. Am. Chem. Soc.*, 2008, **130**, 8261–8270.
8 S. P. Thompson, J. E. Parker, J. Potter, T. P. Hill, A. Birt, T. M. Cobb, F. Yuan and C. C. Tang, *Rev. Sci. Instrum.*, 2009, **80**, 879.
9 I. Puente-Orench, J. F. Clergeau, S. Martínez, M. Olmos, O. Fabelo and J. Campo, *J. Phys.: Conf. Ser.*, 2014, **549**, 012003.
10 E. Suard and A. Hewat, *Neutron News*, 2001, **12**, 30–33.
11 J. A. Rodríguez-Velamazán, J. Campo, J. Rodríguez-Carvajal and P. Noguera, *J. Phys.: Conf. Ser.*, 2011, **325**, 012010.
12 M. Lü, O. Mentré, E. E. Gordon, M. H. Whangbo, A. Wattiaux, M. Duttine, N. Tiercelin and H. Kabbour, *J. Magn. Magn. Mater.*, 2017, **444**, 147–153.
13 R. D. Smyth, J. A. D. Wilson, P. Manuel and S. J. Clarke, *J. Solid State Chem.*, 2022, **307**, 122841.
14 G. Shirane, *Acta Crystallogr.*, 1959, **12**, 282–285.
15 R. K. Oogarah, E. Suard and E. E. McCabe, *J. Magn. Magn. Mater.*, 2018, **446**, 101–107.
16 L. L. Zhao, S. Wu, J. K. Wang, J. P. Hodges, C. Broholm and E. Morosan, *Phys. Rev. B: Condens. Matter Mater. Phys.*, 2013, **87**, 020406(R).
17 E. E. McCabe, C. Stock, E. E. Rodrigues, A. S. Wills, J. W. Taylor and J. S. O. Evans, *Phys. Rev. B: Condens. Matter Mater. Phys.*, 2014, **89**, 100402(R).
18 M. H. Whangbo, E. E. Gordon, H. Xiang, H. J. Koo and C. Lee, *Acc. Chem. Res.*, 2015, **48**, 3080–3087.
19 Y. Fuwa, M. Wakeshima and Y. Hinatsu, *J. Phys.: Condens. Matter*, 2010, **22**, 346003.
20 D. Berthebaud, O. I. Levedev, D. Pelloquin and A. Maignan, *Solid State Sci.*, 2014, **36**, 94–100.
21 B. C. Sheath, X. Xu, P. Manuel, J. Hadermann, M. Batuk, J. O'Sullivan, R. S. Bonilla and S. J. Clarke, *Inorg. Chem.*, 2022, **61**, 12373–12385.